ELSEVIER

Contents lists available at ScienceDirect

Earth and Planetary Science Letters

www.elsevier.com/locate/epsl



Long-lived (ca. 22–24 Myr) partial melts in the eastern Himalaya: Petrochronologic constraints and tectonic implications



Huixia Ding a,*, Matthew J. Kohn b, Zeming Zhang a,c

- ^a School of Earth Sciences and Resources, China University of Geosciences, Beijing, 100083, China
- ^b Department of Geosciences, Boise State University, Boise, ID 83725, United States
- ^c Institute of Geology, Chinese Academy of Geological Sciences, Beijing, 100037, China

ARTICLE INFO

Article history: Received 15 June 2020 Received in revised form 11 January 2021 Accepted 12 January 2021 Available online 22 January 2021 Editor: A. Yin

Keywords: monazite zircon petrochronology P-T path anatexis Himalaya

ABSTRACT

Partial melting is thought to profoundly impact the rheology and deformation behavior of the middle crust. Consequently, investigations of the pressure-temperature conditions of metamorphism, rates of heating, and durations of anatexis can provide unique constraints on tectonic processes. The Greater Himalayan Sequence (GHS), in the metamorphic core of the Himalayan orogen, is commonly considered to represent exhumed, anatectic, mid-crust. Here, we present detailed petrological and geochronological analysis of anatectic pelitic schist and felsic paragneiss from the uppermost structural level of the GHS to understand the timing and conditions of Himalayan anatexis. Petrologic analysis indicates that these rocks experienced high-grade metamorphism and partial melting up to peak conditions of ca. 720-745°C and ca. 9.6-10 kbar. Melt volumes of ca. 3% increased slightly during exhumation with nearly constant or slightly decreasing temperature, then decreased as rocks cooled, ultimate crossing the solidus at ca. 5.5 kbar and 700°C. Well-correlated U-Th-Pb ages and trace element data (HREE, Y, and Eu/Eu*) for monazite and zircon require prograde metamorphism and initial partial melting of GHS rocks at ca. 50 and 42-40 Ma, respectively, and crystallization of melts at ca. 24-18 Ma. These data indicate a long-lived (ca. 22-24 Myr) partially molten mid-crust in the eastern Himalayan orogen that formed as much as 10 Myr earlier and lasted 10 Myr longer than numerical models of viscous flow have predicted. Thermal buffering and melt stagnation may reflect feedbacks between thermal structure and shear stress. The change from thermal and mechanical stasis to rapid exhumation and cooling at ca. 24 Ma corresponds with an orogen-wide shift in deformation patterns, and may reflect arrival of mainland India.

© 2021 Elsevier B.V. All rights reserved.

1. Introduction

Partial melting of middle to lower crust in an orogen results in the formation of melt, which lowers the crustal viscosity and weakens the crust and strongly affects the architecture and behavior of mountain belts, including shaping orogenic plateaus, nucleating convergent and divergent structures, and fostering the formation of gneiss domes (e.g., Teyssier and Whitney, 2002; Cook and Royden, 2008; Jamieson et al., 2011). Thus, the timing and duration of crustal melting in an orogen are of fundamental importance to its thermal and structural evolution. Exposed Himalayan rocks record widespread partial melting (see summary of Weinberg, 2016), while geophysical investigations indicate that the middle crust of the Tibetan Plateau is partially molten today (Nelson et al., 1996). Because of such extensive evidence for partial melting,

* Corresponding author. E-mail address: dhx1987105@126.com (H. Ding). both in the past and today, the Himalaya is commonly considered as the type example of hot orogens (Beaumont et al., 2006).

Widespread exposures of migmatitic Greater Himalayan Sequence (GHS) rocks are the principal basis for inferring past partial melts in the Himalaya. These rocks represent a thick (up to >20 km), laterally extensive (up to 2000 km) composite sheet of middle crust, which was assembled along one or several thrusts and shear zones within the GHS starting by at least 25 Ma (e.g., Kohn et al., 2004; Goscombe et al., 2006; Montomoli et al., 2015; Larson et al., 2015; Carosi et al., 2018). At the orogen-scale, the persistence of these rocks along- and across-strike has given rise to models that depend on protracted viscous flow (e.g., channel flow; Beaumont et al., 2001). The generation of these widespread melts, and timing of their formation, have also been used to illuminate mechanisms by which granite belts form (Le Fort, 1975; Harrison et al., 1998; Weinberg, 2016). Thus, the GHS offers an excellent opportunity to study the interplay between melting and orogenic processes.

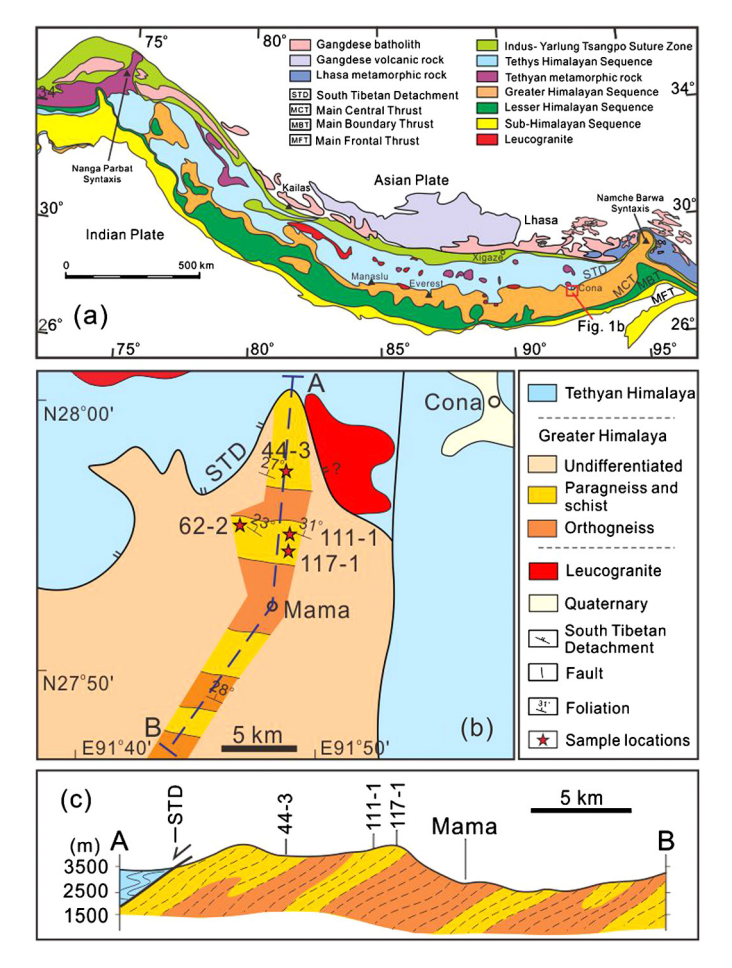


Fig. 1. (a) Schematic geological map of the Himalayan orogen (modified after Yin and Harrison, 2000; Guillot et al., 2008), showing overall geology and general location of the Cona area near the boundary between GHS and THS rocks (upper structural level of the Greater Himalayan Sequence) in the eastern Himalaya; (b) Geological map of the Cona area, China, showing approximate sampling sites and location of cross section (blue dashed line); (c) Cross section in the Cona area. (For interpretation of the colors in the figure(s), the reader is referred to the web version of this article.)

In this paper, we investigate schist and paragneiss from the upper GHS in the Cona area, eastern Himalaya, China (Fig. 1) to better understand the P-T conditions, timing, and duration of partial melting in the uppermost levels of the Himalayan metamorphic core in the region. We first characterize the petrology of metapelite and felsic gneiss. In addition to key textures and chemical systematics, we determine peak P-T conditions and construct a P-T path. We then document coupled U-Th-Pb ages and trace element data of monazite and zircon in these rocks. While Ding et al. (2017) have reported basic petrologic data and cooling ages for the orthogneiss in the study area, we now provide extensive new models, trace element data, geochronologic data, and interpretations of the initiation age of prograde metamorphism, timing of partial melting, and timing of melt crystallization. Finally, we explore the implications of these long-lived partial melts for orogen-scale tectonic models.

2. Geological setting

The Himalaya formed as a result of collision between India and Asia at ca. 60–50 Ma (e.g., Najman et al., 2010; Hu et al., 2015; Kapp and DeCelles, 2019 and references therein), which is bounded by the Indus–Yarlung Tsangpo Suture zone to the north and the Main Frontal Thrust (MFT) to the south. Rocks of the Himalaya are commonly divided into four roughly parallel, laterally continuous,

litho-tectonic units. From north to south, these are the: Tethyan Himalayan Sequence (THS), Greater Himalayan Sequence (GHS), Lesser Himalayan Sequence (LHS), and Sub-Himalayan Sequence (SHS) (Fig. 1a; Yin and Harrison, 2000). These units are separated by the South Tibetan Detachment System (STDS; THS-GHS), Main Central Thrust (MCT; GHS-LHS) and Main Boundary Thrust (MBT; LHS-SHS) (Fig. 1a; Yin and Harrison, 2000). Focusing on the GHS, additional thrusts and shear zones have been proposed within it, notably, the Higher Himalayan Discontinuity (HHD; e.g., Kohn et al., 2004; Goscombe et al., 2006; Cottle et al., 2015; Montomoli et al., 2015; Carosi et al., 2018). Thrust-sense displacement along the HHD (or its locally-named shear zone) is interpreted to have occurred as early as ca. 25 Ma, while movement on the MCT may have initiated as late as ca. 17 Ma (see summary of Carosi et al., 2018).

The GHS represents the metamorphic core of the orogen and consists of amphibolite- to granulite-facies metamorphic rocks and leucogranites. Metasedimentary rocks of the lower GHS record an inverted, Barrovian-type, metamorphic field gradient, such that metamorphic grade increases from kyanite to sillimanite + K-feldspar structurally upward toward the hinterland (Le Fort, 1975; Kohn, 2014). In addition to metapelitic rocks, subordinate quartzite, calc-silicate and marble also occur in this subunit. The upper portion of the GHS consists mainly of orthogneiss and minor kyanite/sillimanite migmatite, intruded by Miocene leucogranites (Le Fort, 1975).

The Cona area, eastern Himalaya, exposes rocks of the upper GHS (Fig. 1b, c) including granitic orthogneiss with a Neoproterozoic to Late Cambrian protolith age (Ding and Zhang, 2016) and kyanite- and sillimanite-bearing pelitic schists and paragneisses (Fig. 1c). These rocks are cut by minor leucocratic dikes and sills, and their foliation dips gently to NNE (20–30°N) (Fig. 1b). The STDS and a leucogranite intrusion crop out immediately to the north and northeast, respectively (Fig. 1b), of our sample localities, but the structural relationship of the leucogranite to the STDS is unknown.

The GHS is now commonly interpreted as an in-sequence thrust dominated unit that experienced thickening prior to movement on the MCT (Carosi et al., 2018 and references therein). Because the Cona rocks now occupy the structurally highest level of the GHS in the region, they may represent rocks that were metamorphosed farther to the north and earlier than structurally lower GHS. Thus, the Cona rocks provide an opportunity to examine relatively early stages of internal thickening and metamorphism of the GHS.

3. Petrology

The pelitic schists (samples 44-3, 111-1, and 117-1) and felsic paragneiss (sample 62-2) that we studied were collected from the uppermost structural level of the GHS in the Cona area; faults or shear zones do not apparently separate these samples (Fig. 1b, c). The schists and paragneiss are foliated with sparse 1–5 cm-scale leucocratic segregations that are parallel to the foliation (Appendix Fig. 1a, b). Leucosome in both schist and paragneiss consists of plagioclase and quartz. Distinct whole-rock compositions (Appendix Table 1) and differences in the progress of reactions at high-T and during cooling affect mineral textures and assemblages. Analytical methods of bulk rock compositions and mineral compositions are presented in Appendix A. Characteristic textures and assemblages for each sample are as follows:

Sample 44-3. This Grt-Sil schist contains garnet, K-feldspar, muscovite, sillimanite, biotite, plagioclase, quartz as well as minor ilmenite and rutile (Fig. 2a, b). Oriented mica laths, sillimanite needles, and ribbons of plagioclase and quartz define the foliation. The subhedral and poikiloblastic garnet contains abundant inclusions of plagioclase, biotite, quartz and muscovite, and is partly replaced

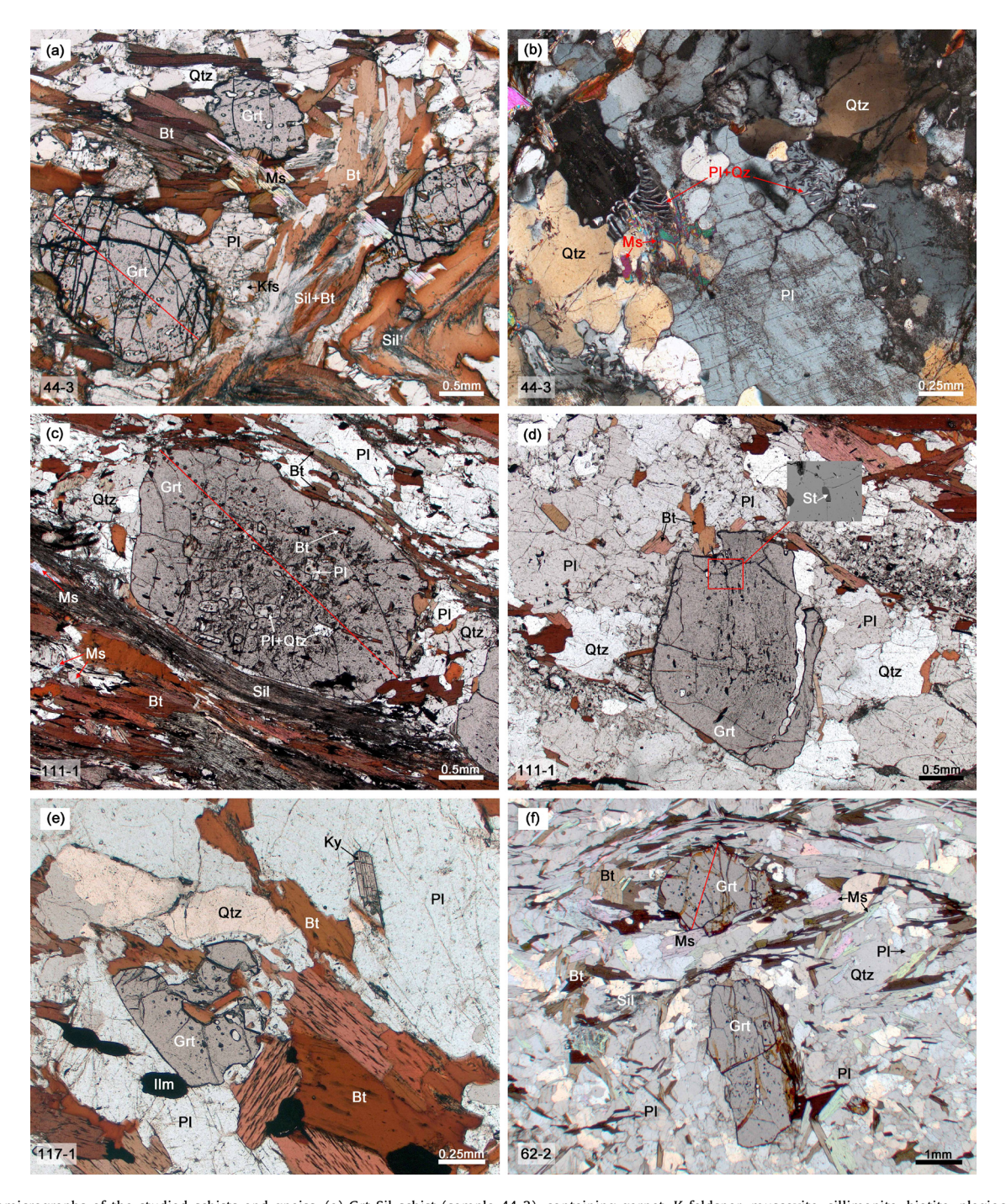


Fig. 2. Photomicrographs of the studied schists and gneiss. (a) Grt-Sil schist (sample 44-3), containing garnet, K-feldspar, muscovite, sillimanite, biotite, plagioclase, quartz, ilmenite and rutile; (b) Myrmekite consisting of plagioclase and quartz surrounding large plagioclase grains (sample 44-3), representing the crystallized former melt; (c and d) Grt-Sil schist (sample 111-1), consisting of garnet, staurolite, muscovite, sillimanite, biotite, plagioclase, quartz and ilmenite. Note that the staurolite occurs only as inclusions within garnet, and the garnet rim is partly replaced by biotite, sillimanite and plagioclase; (e) Grt-Ky schist (sample 117-1), consisting of garnet, muscovite, sillimanite, kyanite, biotite, plagioclase, quartz and ilmenite. Note that the garnet is partly replaced by biotite and plagioclase, and some biotite is partly replaced by sillimanite; (f) Grt-bearing gneiss (sample 62-2), containing garnet, sillimanite, muscovite, plagioclase, quartz, ilmenite and tourmaline. The red lines crossing garnet grains in (a), (c) and (f) refer to the locations of compositional profiles and one in (c) is shown in Fig. 3. The mineral abbreviations used in this paper are as follows: Ab=albite, Alm=almandine, Amp=amphibole, And=andalusite, Bt=biotite, Crd=cordierite, Grs=grossular, Grt=garnet, Ilm=ilmenite, Ky=kyanite, Liq=melt, Mnz=monazite, Ms=muscovite, Pl=plagioclase, Prp=pyrope, Qtz=quartz, Rt=rutile, Sil=sillimanite, Spe=spessartine, St=staurolite and Zrn=zircon.

by biotite, sillimanite and plagioclase along its edges and by biotite along the fractures (Fig. 2a). Vermicular intergrowths of plagioclase and quartz around subhedral plagioclase crystal are present in the matrix (Fig. 2b).

Sample 111-1. This Grt-Sil schist contains a matrix assemblage of garnet, muscovite, sillimanite, biotite, plagioclase, quartz and ilmenite with a distinct schistosity defined by oriented biotite and sillimanite and by elongated plagioclase and quartz (Fig. 2c). The poikiloblastic garnets have inclusion-rich core and inclusion-poor rim. The inclusions in garnet are quartz, plagioclase, biotite, muscovite, chlorite and, notably, staurolite (Fig. 2c, d). The rim is partly replaced by biotite, sillimanite and plagioclase (Fig. 2c, d). No paragonite is observed, which is relevant to our interpretation of pseudosections and the prograde P-T path.

Sample 117-1. This Grt-Ky schist contains a matrix assemblage of garnet, muscovite, sillimanite, biotite, plagioclase, quartz and ilmenite (Fig. 2e). Kyanite also occurs as sparse inclusions in plagioclase (Fig. 2e). The garnet is partly replaced by biotite and plagioclase, while sillimanite partly replaces biotite.

Sample 62-2. This Grt-bearing gneiss contains a matrix assemblage of garnet, sillimanite, muscovite, biotite, plagioclase, quartz and minor ilmenite and tourmaline (Fig. 2f). Poikiloblastic garnet has inclusions of plagioclase and quartz, and is partly replaced by biotite along edges and fractures.

Three generations of mineral assemblages can be distinguished for the schists based on textures and replacing relationships among minerals. A prograde assemblage (M1) is represented by garnet cores and their mineral inclusions: $\operatorname{Grt}(\operatorname{core}) + \operatorname{Pl} + \operatorname{Bt} + \operatorname{Ms} + \operatorname{Qtz} + \operatorname{St}(\operatorname{in sample 111-1 only})$. The maximum pressure assemblage (M2) is $\operatorname{Grt}(\operatorname{mantle}) + \operatorname{Pl} + \operatorname{Bt} + \operatorname{Ms} + \operatorname{Qtz} + \operatorname{Ky}(\operatorname{in sample 117-1 only}) + \operatorname{Ilm} + \operatorname{Rt}(\operatorname{in sample 44-3 only})$. The retrograde assemblage (M3) is characterized by the appearance of sillimanite that replaces garnet edges and biotite. For the gneiss, all minerals except late sillimanite coexist in chemical equilibrium, and its peak mineral assemblage is $\operatorname{Grt} + \operatorname{Pl} + \operatorname{Bt} + \operatorname{Ms} + \operatorname{Qtz} + \operatorname{Ilm}$.

Mineral chemical compositions of the two schists (sample 111-1 and 44-3) and the gneiss (sample 62-2) are presented in Appendix Tables 2-4. Key compositional characteristics include:

Plagioclase (Appendix Table 2). Matrix plagioclase compositions have $X_{An}=0.24$ –0.30 (sample 111-1) and 0.22–0.24 (sample 44-3), whereas plagioclase inclusions (sample 111-1) have relatively high $X_{An}=0.27$ –0.38. For the gneiss (sample 62-2), two analyses of matrix plagioclase have $X_{An}=0.19$.

Biotite (Appendix Table 3). Biotite in all rocks has compositions with average Fe/(Fe+Mg) = 0.63 (schist 44-3), 0.61 (schist 111-1 inclusions in garnet) to 0.69 (schist 111-1 matrix), and 0.64 (gneiss 62-2), and average TiO_2 content of 2.80 wt% (sample 44-3), 2.70 wt% (sample 111-1 inclusions) to 3.11 wt% (sample 111-1 matrix), and 2.94 wt% (sample 62-2).

Muscovite (Appendix Table 3). Matrix muscovite compositions vary slightly among all rocks, with average of Si = 3.09, 3.14, 3.10 cations per formula unit and average of Fe/(Fe+Mg) = 0.59, 0.63, 0.55 for samples 44-3, 111-1, and 62-2, respectively. Inclusion muscovite in sample 111-1 has a slightly higher Si = 3.20 cations, but similar Fe/(Fe+Mg) = 0.58.

Staurolite (Appendix Table 3). The staurolite inclusion in the garnet from schist sample 111-1 has Fe/(Fe+Mg) = 0.84.

Garnet (Appendix Table 4). Compositional zoning across garnet from all samples shows slightly decreasing spessartine and constant almandine contents from the core towards the rim, and a sharp increase in spessartine at the rim (Fig. 3). Grossular content increases slightly from the core towards the rim in samples 44-3 and 111-1, and shows a slight decrease close to garnet rims in sample 111-1 with a small increase at the outmost rim on one side of the garnet. Grossular content is generally invariable throughout garnet in sample 62-2. Garnet next to the staurolite inclusion has

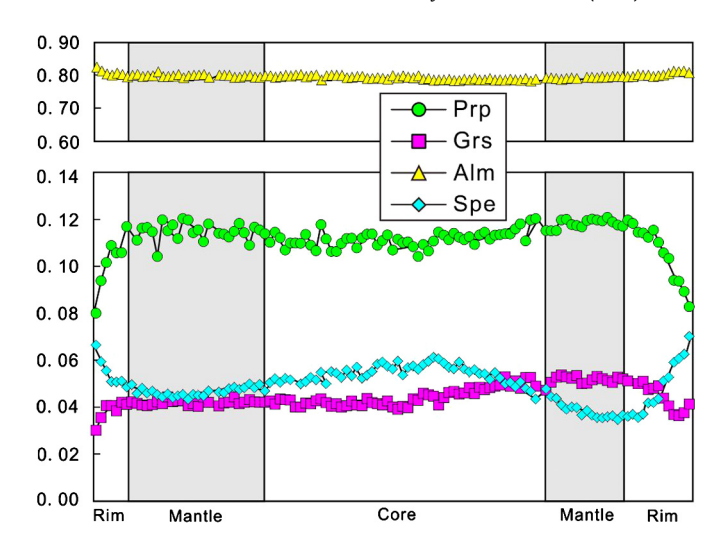


Fig. 3. Garnet compositional profile (sample 111-1), representing rim-to-rim analyses through garnet porphyroblast. Pyrope component increases slightly from core toward mantle, then decreases at rim; grossular on right-hand rim shows small oscillation. Spessartine component shows small decrease towards rim, then increases at rim. This compositional zoning is consistent with diffusionally-modified prograde garnet growth (core-towards rim), followed by garnet resorption plus reequilibration (rim zoning).

similar spessartine content (0.05) to the core of the garnet in sample 111-1.

4. Metamorphic conditions and P-T path

Metamorphic P–T conditions of sample 111-1 were constrained by phase equilibria modeling and garnet–plagioclase–sillimanite–quartz barometry (Koziol, 1989); analytical and computational methods are presented in Appendix A. A P–T pseudosection (Fig. 4a) was constructed based on the measured bulk rock composition (Appendix Table 1) over a P–T range of 3–12 kbar and 400–800°C. In the calculated P–T range, garnet is always present (Fig. 4c), but its mode is small at low pressures (blue field). Plagioclase is stable except for the upper left corner (Fig. 4d). Staurolite is stable within a narrow field of T < 650°C and P < 7.5 kbar (the thick yellow line in Fig. 4a, b). Kyanite is stable over a wide range of P–T conditions of above 3 kbar and 440°C and 10 kbar and 800°C. The solidus of the system is located at 680–725°C.

The early prograde assemblage (M1) in this rock, observed via inclusions (Grt + Pl + Bt + Ms + Qtz + St), is stable over a P-T range of $T = 400-650^{\circ}C$ and P = 3-7.5 kbar (Fig. 4a), which represents the prograde nucleation and early growth conditions of the garnet. The decreasing spessartine from core to mantle of the garnet (Fig. 3) is generally consistent with growth zoning, but the relatively flat profiles suggest substantial diffusional homogenization, likely near the peak of metamorphism. Because original garnet (and likely staurolite) compositions are not preserved, we cannot pin down the P-T conditions of this assemblage more precisely.

The reversals in spessartine and pyrope zoning between the mantle and rim are consistent with back reaction and diffusional modification of the garnet rim during cooling. Therefore, the mantle of the garnet should most closely approximate compositions that formed at the peak condition. Because the anorthite content of plagioclase decreases as garnet grows (e.g., Spear et al., 1991), plagioclase with the lowest X_{An} is commonly regarded as most closely approximating conditions at maximum garnet mode. Furthermore, biotite develops higher Ti content with increasing T (e.g., Henry et al., 2005), so biotite with the highest Ti content is commonly interpreted to have formed at the peak temperature. Based on these rationales, we interpret the garnet mantle with troughs in X_{Spe} ,

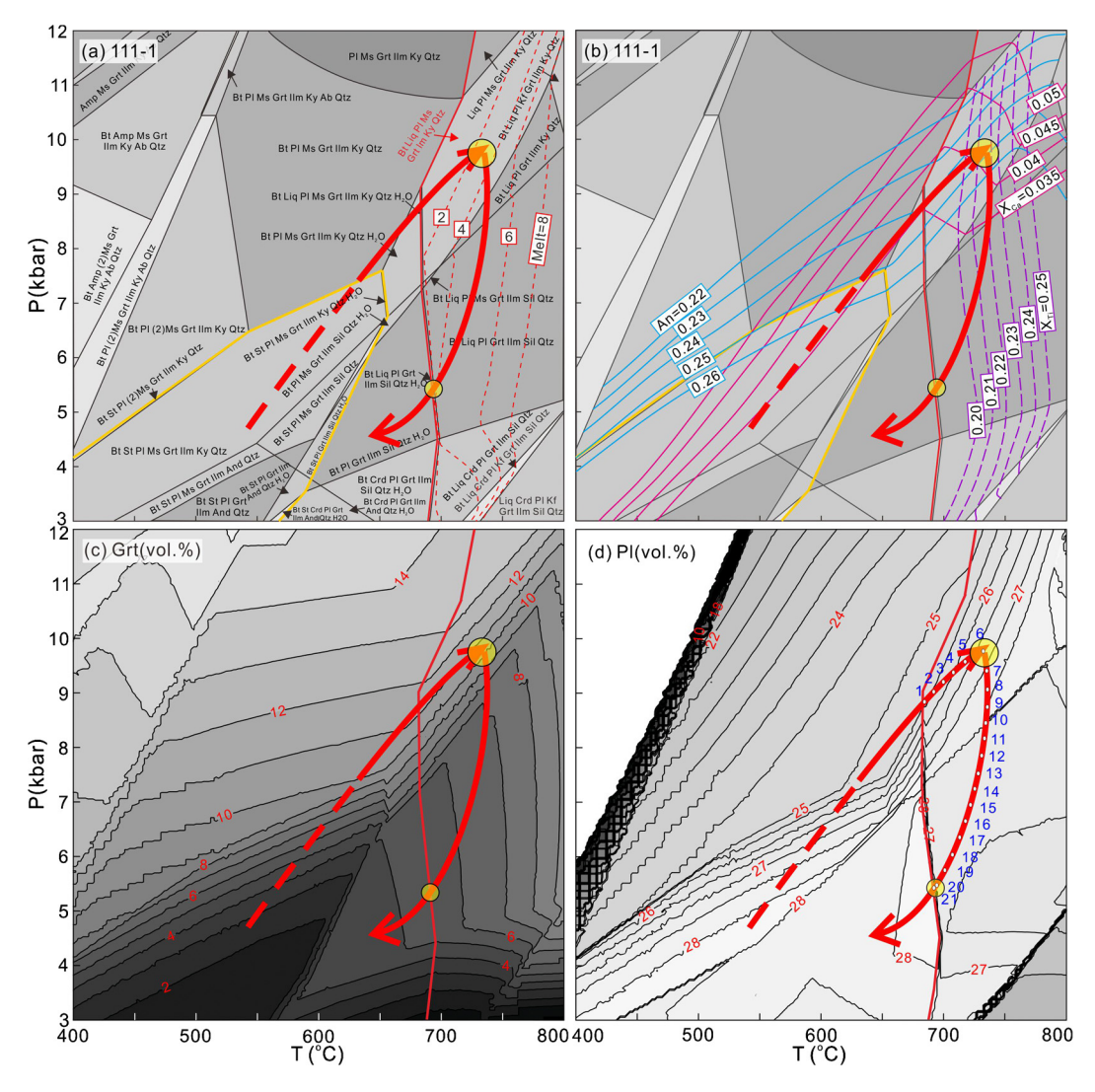


Fig. 4. P-T pseudosection (a and b), and isomodes of garnet (c) and plagioclase (d) of the studied metapelite (sample 111-1). The yellow line represents the staurolite-in line. The thin full red line represents the solidus of the system, and the thin red dashed lines are the melt isomodes (in vol.%). The thick red line with arrow is the inferred P-T path. The larger circle filled with the yellow color represents peak P-T condition constrained by compositional isopleths of garnet $[X_{Ca} = Ca]/(Fe^{2+} + Mg + Ca + Mn)]$, plagioclase $[X_{An} = Ca]/(Na + Ca + K)]$ and biotite $[X_{Ti} = Ti]$. The semi-transparent small circle filled with the yellow color represents retrograde P-T condition calculated using geobarometry. The red numbers in (c) and (d) are mineral abundances. The tiny white ellipses in (d) are the locations where monazite and zircon contents are calculated (see Fig. 9). Note that near-solidus plagioclase contours are densely-distributed and with larger contour value towards the solidus.

plagioclase with the lowest X_{An} , and biotite with the highest X_{Ti} as best representing compositions at the metamorphic peak.

For estimating maximum pressure M2 metamorphic conditions, we note that: 1) the grossular component in garnet is asymmetrically zoned, with values of 0.04 to 0.05 in the mantle region, 2) the mole fraction of anorthite (from plagioclase inclusions) is higher in the garnet core (An_{27-38}) than in the matrix (An_{24-30}) , and 3) the TiO₂ content of biotite increases from inclusions in the garnet (2.70 wt.%) to matrix grains (3.11 wt.%). Contours for the lowest value for X_{An} (0.24), and highest Ti content for matrix biotite (Ti = 0.23 pfu) intersect at a P-T condition of ca. 720-745°C and ca. 9.6-10 kbar (the upper yellow or pink circle in Fig. 4), which likely approximates the peak P-T conditions of the studied rocks. The intersection point corresponds with $X_{Grs}=0.04$, which is common throughout the mantle region of the garnet, and implies a small amount of melt (ca. 3%; Fig. 4a), consistent with the small proportion of leucosomes we observe in the studied samples (Appendix Fig. 1). Our models also indicate that kyanite was stable. Although kyanite is not observed in this rock, a high abundance of sillimanite may mark its destabilization. For example, nearby sample 111-7 contains abundant sillimanite, but only a single relict grain of kyanite (Fig. 2e). This texturally latest, sillimanite-bearing, M3 assemblage is stable over a wide P–T field of $T=550-800^{\circ}C$ and P=3-10 kbar.

Although we cannot pin down the P-T condition at which sillimanite first formed, more definite P-T conditions of later melt crystallization can be estimated by barometry estimates from Grt-Pl-Sil-Qtz with the (nearly temperature-invariant) solidus. Assuming that the rim composition in the garnet has reequilibrated during exhumation and cooling, rim compositions for all matrix minerals ($X_{Grs} = 0.03-0.04$, $X_{An} = 0.28-0.30$, assuming X_{An} increased during garnet dissolution to maintain Ca mass balance), suggests a final recorded P–T condition of ca. 700 and 5.5 \pm 1 kbar. Connecting this result with peak P-T conditions implies over 4 kbar exhumation with cooling <50°C. Such a P-T path is consistent with a high Ti-content of matrix biotite and the production of abundant sillimanite at the expense of garnet. If the interpretation is correct, isothermal exhumation would increase melt content by only a few percent, reaching a maximum melt content of ca. 5% (Fig. 4a).

Overall, these data suggest a clockwise P–T path characterized by an increase in both P and T to a maximum pressure of ca.

(a) Monazite

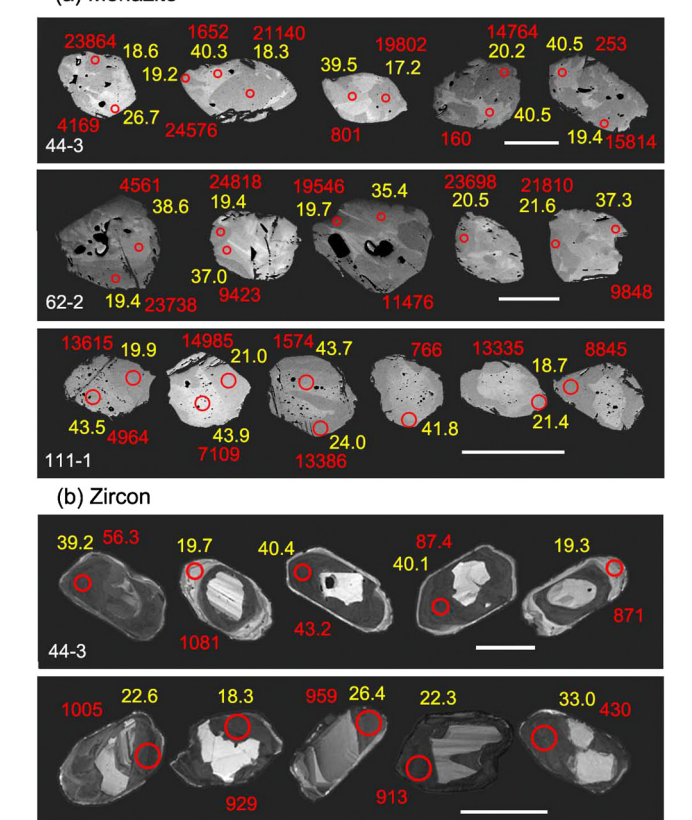


Fig. 5. Back-scattered electron (BSE) images of monazite (a) and cathodoluminescence (CL) images of zircon (b) from the studied rocks, showing the analyzed spot locations and relevant ages (in Ma, yellow number) and Y content (in ppm, red number). The scale bars are 100 μ m.

10 kbar (at 720–745°C) with a melt content of ca. 3%, followed by quasi-isothermal exhumation to a P–T condition of ca. 5.5 kbar and 700°C with a melt content of ca. 5 vol.%.

5. Monazite and zircon geochronology and trace element compositions

Our interpretations of the timing of melting, reaction progress at high temperature, and timing of melt crystallization depend closely on the geochronology and trace element compositions of monazite and zircon. Chronologic reproducibilities on standards were ca. 1% (2σ) so counting statistics errors of ca. 5% dominate uncertainties. Errors on trace element concentrations are generally below 1%. Detailed analytical and computational methods for geochronologic and trace element data collection and interpretation are presented in Appendix A.

The locations of representative monazite and zircon U-Th-Pb dates for samples 111-1, 44-3 and 62-2 are shown in Fig. 5 and Appendix Fig. 2, and the isotope data, ages, and trace element data are presented in Appendix Tables 5 and 6, Appendix Figs. 3 and 4, and Fig. 6. As described next, age and geochemical data for monazite (section 5.1) and zircon (section 5.2) can be divided into two groups corresponding to ages >40 Ma, and ages <40 Ma.

5.1. Monazite

Monazite ages were determined from in situ analyses both in separated grains and in thin section. Grains in thin section mostly occur as inclusions in biotite and plagioclase, although a few are found in garnet (Appendix Table 5). The ages for inclusions in biotite and plagioclase span nearly the entire age range, whereas the small number of grains in garnet cluster towards younger ages. Most monazite is irregularly zoned and exhibits BSE-bright and -dark domains (Fig. 5a; Appendix Fig. 2), although some are unzoned.

For any one monazite grain, the BSE-dark domains tend to have relatively high Y, low Ca and U, and young Th-Pb ages, whereas the BSE-bright domains have relatively low Y, high Ca and U, and old Th-Pb ages (Fig. 5a; Appendix Fig. 2). Unzoned monazite commonly has similar characteristics to the BSE-dark domains. All of the analytical spots yield concordant or nearly concordant ²⁰⁸Pb/²³²Th - ²⁰⁶Pb/²³⁸U ages ranging from 46.2 Ma to 13.3 Ma (Appendix Fig. 3, Appendix Table 5). The BSE-bright domains with ages of ca. 40-46 Ma have distinctively low concentrations of heavy rare earth elements (HREE, 6.60-352 ppm except two spots with 438 and 683 ppm) and Y (160-8943 ppm) that decrease with decreasing age. Eu/Eu* shows moderate to high values (0.36-0.62) that increase with decreasing age. Domains with ages of 39–13 Ma show the opposite trend; concentrations of HREE (154–2656 ppm) and Y (2485–25364 ppm) markedly increase with decreasing age, while Eu/Eu* decreases (0.11-0.60; Fig. 6a-c). Notably, Eu/Eu* sharply decreases between 22 Ma to 13 Ma (Fig. 6c), and a 7-point running average of Y illustrates the reversal in Y trend at ca. 41 Ma (Fig. 7).

5.2. Zircon

Zircon was analyzed only as separated grains. Most zircon grains show core–mantle–rim structure in Cathodoluminescence (CL) images (Fig. 5b). Textural cores have variable size, shape, and zoning, and are interpreted to be inherited. Mantles show weak patchy zoning with lower CL intensity. Rims exhibit more pronounced patchy zoning with higher CL intensity (Fig. 5b). Only a few rims are sufficiently wide to collect LA–ICP–MS U–Pb ages and trace element compositions.

The mantles and rims of zircons show low and variable Th/U values (0.005–0.022) and REE contents (21.5–1014 ppm) and weakly fractionated to flat HREE patterns with negative Eu anomalies (Appendix Fig. 4; Appendix Table 6). All U–Pb ages are concordant and range from 49.7 Ma to 18.1 Ma (Appendix Fig. 4; Appendix Table 6). The domains with ages of ca. 40–50 Ma have very low concentrations of HREE (4.89–49.5 ppm) and Y (25.6–110 ppm) and high and variable Eu/Eu*(0.19–0.54), whereas domains with ages of 39–18 Ma show increasing concentrations of HREE (9.02–906 ppm) and Y (48.6–1083 ppm) and decreasing Eu/Eu* (0.10–0.86) with decreasing ages (Fig. 6d–e; Appendix Table 6).

Combined age data for monazite and zircon show a nonuniform age distribution with peaks at ca. 41 Ma and 19 Ma (Fig. 7).

6. Discussion

6.1. Initiation and duration of partial melting of Himalayan middle crust

Nearly all studies of the initiation and duration of anatexis in the GHS correspond with the central and western Himalaya of Nepal and India, not the eastern sector of the Himalaya (e.g., Weinberg, 2016). Whereas Ding et al. (2017) reported briefly on the timing (27–11 Ma) of cooling at Cona, they did not constrain the timing of partial melting, which is key to this study. Many researchers view partial melting of GHS rocks to have been restricted to 25–15 Ma (see summary of Weinberg, 2016). However, our data as well as other studies (e.g., Carosi et al., 2015) suggest the GHS reached partial melting conditions much earlier and resided much longer in the partial melt field.

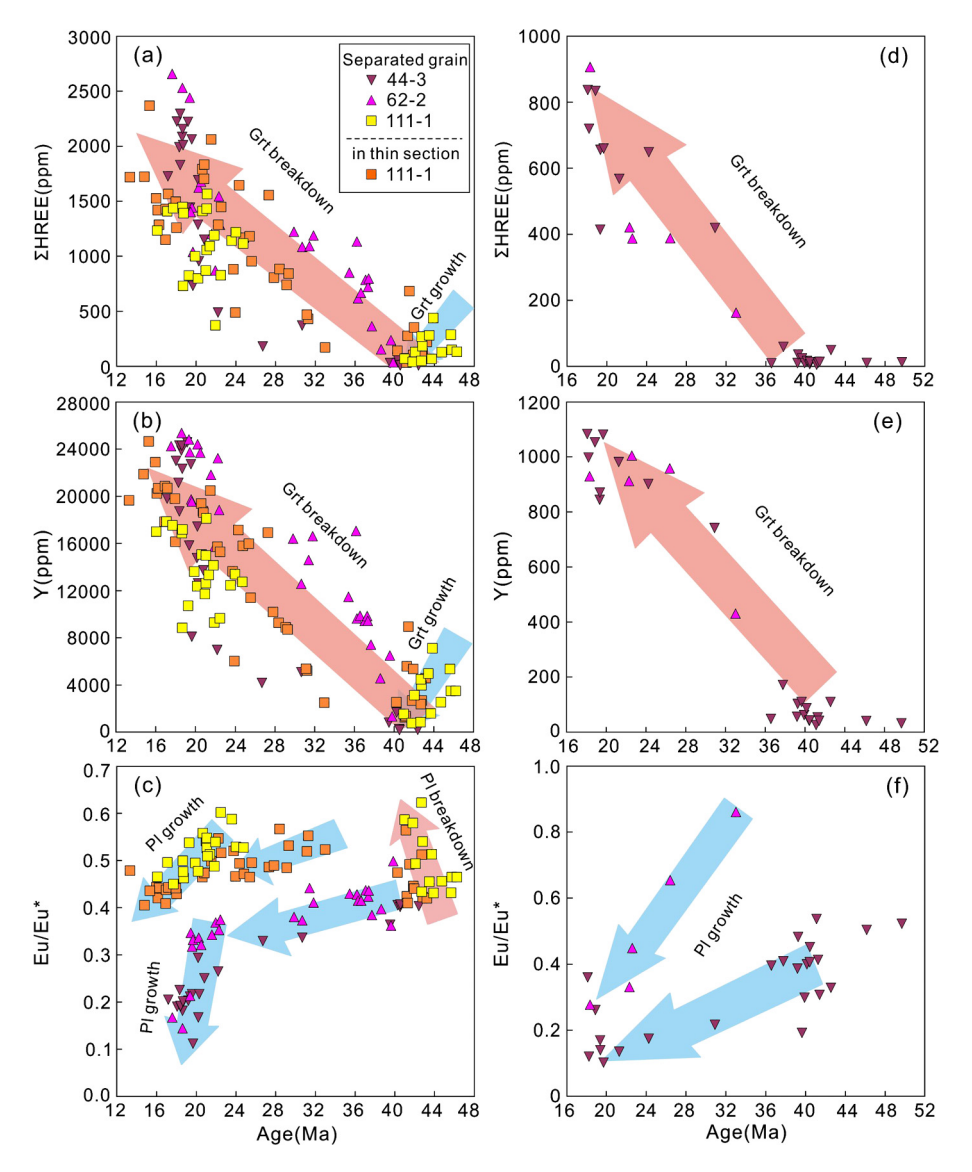


Fig. 6. Diagrams of HREE, Y, Eu/Eu* vs. age of monazite (a-c) and zircon (d-f) of the studied rocks. The analyzed domains can be divided into two group based on the opposite geochemical features. The domains with ages \geq 40 Ma have low HREE and Y content and show gradual decreases in HREE (a) and Y (b) and increases in Eu/Eu* (c) with decreasing age, indicating garnet growth and feldspar breakdown, respectively, during the pre-melting stage. The domains with ages <40 Ma have high HREE and Y contents and progressive increases in HREE (a and d) and Y (b and e) and decreases in Eu/Eu* (c and f) with decreasing age, indicating they grew during garnet breakdown and feldspar consumption. The reversal in compositional trends ca. 42–40 Ma can be regarded as the timing of initiation of the partial melting. See also Fig. 7 for Y trends.

Decreasing HREE and Y with decreasing age to 40-42 Ma for the oldest monazite in 111-1 (Fig. 6a, b; Appendix Table 5) is consistent with progressive depletion of the matrix in these components as garnet grew (e.g., Rubatto, 2002; Pyle and Spear, 2003; Rubatto et al., 2013). If so, ages for monazite and zircon as high as 50 Ma should approach the age of garnet nucleation (Fig. 8). This interpretation accords with other studies indicating metamorphism of the GHS initiating as early as ca. 48 Ma (Ding et al., 2016). Increasing Eu/Eu* for sample 111-1 (Fig. 6c) is consistent with plagioclase breakdown (Rubatto et al., 2013; Wang et al., 2015). For the studied rocks, K-feldspar is negligible (occurs only in sample 44-3), so Eu/Eu* trends are likely related to growth and consumption of plagioclase rather than K-feldspar. Whereas the early trends towards decreasing HREE and Y, and increasing Eu/Eu* for sample 111-1 (Fig. 6a-c) are less well defined, they accord with pseudosection models that predict growth of garnet and consumption of plagioclase (Fig. 4c. d).

With decreasing age, HREE and Y reverse from decreasing to increasing while Eu/Eu* reverse from increasing to decreasing (Figs. 6, 7). Both reversals occur at 40–42 Ma and mark a switch

from garnet growth to garnet breakdown, and from plagioclase breakdown to plagioclase growth (Rubatto, 2002). Petrologically, this switch occurs at the partial melting reaction at ca. 700°C (Fig. 4c, d). Thus, the changes in the HREE, Y, and Eu/Eu* trends at 40–42 Ma mark the onset of partial melting at ca. 700°C in these rocks (Fig. 8). In the east-central Himalaya, leucogranites are as old as ca. 44 Ma (Aikman et al., 2008) and Eocene (41–36 Ma) anatectic melt inclusions have been found in garnet of the GHS (Carosi et al., 2015). Although we find no evidence for extraction of melts as early as 44 Ma in the study area, these data imply partial melting in the Himalaya at least as early as we infer in the Cona area.

Increasing HREE and Y, and decreasing Eu/Eu* between 40 and at least 18 Ma (zircon), possibly as young as 13 Ma (monazite), suggest progressive consumption of garnet and growth of plagio-clase. Either prograde melting or exhumation (or both) could drive plagioclase growth and garnet consumption (Fig. 4c, d), but most empirical studies and modelling indicate that monazite and zircon in anatectic rocks commonly dissolve during partial melting and grow during cooling and melt crystallization (Fig. 9; Pyle and

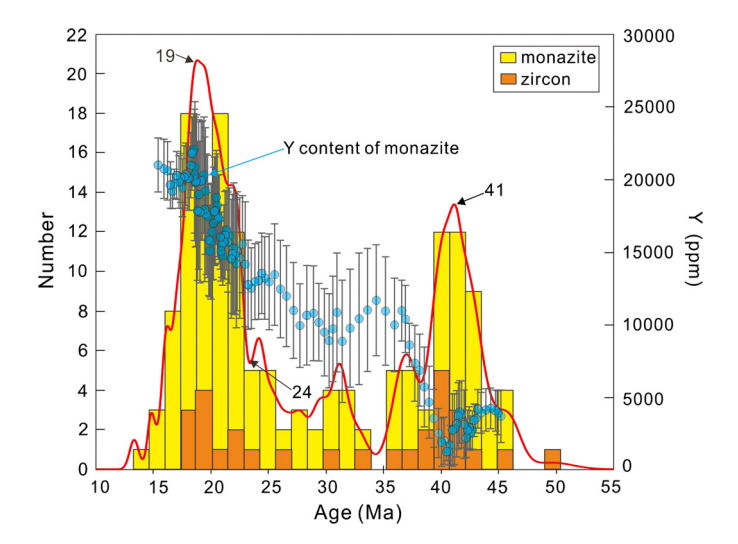


Fig. 7. Probability distributions of monazite and zircon ages and 7-point running average of Y content (error bars correspond with standard error of 7-analysis window). The intervals of 50-42 Ma and 24-18 Ma represent the pre-melting prograde stage and melt crystallization, respectively. A reversal in the Y trend is evident at ca. 41 Ma and likely marks the timing of initial melting. We do not interpret possible reversals at 35 and 30 Ma because error bars are large.

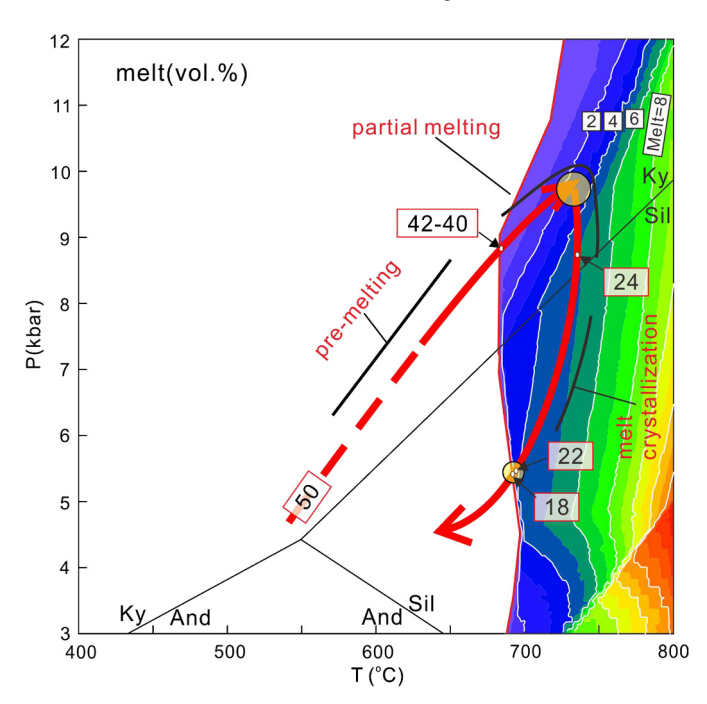


Fig. 8. P-T-t path of the studied rocks, indicating that metamorphism, partial melting and melt crystallization initiated at ca. 50 Ma, ca. 42–40 Ma and ca. 24 Ma, respectively, and that melt crystallization ended at 18 Ma. The melt mode increases from the cool colors to the warm colors. The larger and small circles filled with the yellow color represent peak and retrograde P-T conditions, respectively. The mineral assemblages for melt crystallization stage (24–18 Ma) is Grt + Bt + Pl + Sil or Ky + Otz + Ilm + melt.

Spear, 2003; Kohn et al., 2005; Kelsey et al., 2008). The age probability diagram shows an increase in the number of ages commencing at ca. 24 Ma (Fig. 7) and a smaller number of ages ranging from 41 to 24 Ma. In parallel with previous studies (Pyle and Spear, 2003; Kohn et al., 2005; Kelsey et al., 2008), we interpret the peak that begins at ca. 24 Ma to represent melt crystallization. The ages between 41 and 24 Ma then bracket the timing of anatexis (Fig. 8). The sharp Eu/Eu* drop in monazite with ages of ca. 22–13 Ma (Fig. 6c) and densely-distributed contours of plagioclase abundance near the solidus (Fig. 4d) suggest a close approach to

the solidus by 22 Ma (Fig. 8). Monazite can be especially susceptible to growth or alteration from an aqueous fluid (Kirkland et al., 2009; Harlov et al., 2011), and monazite inclusions can reequilibrate to younger ages along cracks (Martin et al., 2007). At least one of the monazite inclusions is adjacent to a crack in the studied rocks (Appendix Fig. 5), so we take the youngest zircon age (18 Ma) as the best estimate of final crystallization of in situ melts (Fig. 8). In addition, the growth of abundant zircon and monazite with ages of ca. 22-18 Ma (Fig. 7) accords with models that suggest a pulse of monazite and zircon growth at the very end of melt crystallization (Fig. 9; Kelsey et al., 2008). The short duration of entire melt crystallization (24-18 Ma) is also consistent with other studies of anatectic rocks in the Himalaya that indicate cooling from peak temperatures to the solidus in \leq 7 Ma (e.g., Rubatto et al., 2013; Iaccarino et al., 2015). As expected, all zircon and monazite crystallization ages exceed 40 Ar/39 År muscovite and biotite cooling ages of 8-12 Ma in GHS gneisses ca. 20 km to the SSW (Yin et al., 2010).

In sum, garnet nucleation, partial melting, and melt crystallization of the studied rocks each initiated at ca. 50 Ma, 40–42 Ma and ca. 24 Ma, respectively. Melt crystallization ended at ca. 18 Ma, pointing to a surprisingly long-time span (ca. 22–24 Myr) for the persistence of partially molten middle crust as represented in the upper GHS. Relatively long durations (15 Myr to >20 Myr) at temperatures above the solidus of metapelites are also indicated in the mid- to upper GHS in central Nepal and southern China (Kohn and Corrie, 2011; Zhang et al., 2015; Wang et al., 2015; Walters and Kohn, 2017).

6.2. Partial melting, weakening, and flow of the GHS

Even small amounts of melt could play an important role in the rheologic behavior of crustal rocks. Experimental studies (e.g., Rosenberg and Handy, 2005) indicate that 5% melt, as modelled for the upper GHS, could decrease the viscosity of the crust by nearly an order of magnitude. Such a large decrease in viscosity could permit enhanced flow of Himalayan middle crust (Beaumont et al., 2001; Jamieson et al., 2004, 2011). However, Rosenberg and Handy (2005) advocate caution in extrapolating high strainrate experiments to natural systems. In their experiments, small melt fractions formed interconnected networks that favored sliding along grain boundaries. In contrast, felsic melts tend to pool at grain boundary intersections (Jurewicz and Watson, 1985), leaving a stronger interconnected framework of crystals. If melts do not wet grain boundaries, small amounts of melt might not induce the dramatic weakening that high strain-rate experiments imply.

High temperatures and the presence of partial melts are thought to weaken the mid- to lower crust sufficiently to induce lateral and upward flow, strongly influencing orogen dynamics (e.g., Beaumont et al., 2001; Teyssier and Whitney, 2002; Cook and Royden, 2008; Jamieson et al., 2004, 2011). For example, lateral flow has been proposed to explain exposure of migmatitic GHS rocks via south-directed flow towards the Himalayan front ("channel flow"; Beaumont et al., 2001), topographic rise of both the Tibetan Plateau and southeast Asia via north- and east-directed flow (e.g., Cook and Royden, 2008), and formation of gneiss domes via upward flow in southern Tibet (Beaumont et al., 2001; Teyssier and Whitney, 2002). In several respects, the P-T-t evolution of the Cona rocks resembles predictions of south-directed channel flow (Jamieson et al., 2004). Both indicate protracted heating above the solidus, rapid cooling at low pressure, and a clockwise P-T path. However, the metamorphic record and models differ in two impor-

First, channel-flow models imply that south-directed flow of the GHS should produce much flatter P–T paths for rocks that reach \sim 720°C, with quasi-isobaric heating between 500 and 700°C

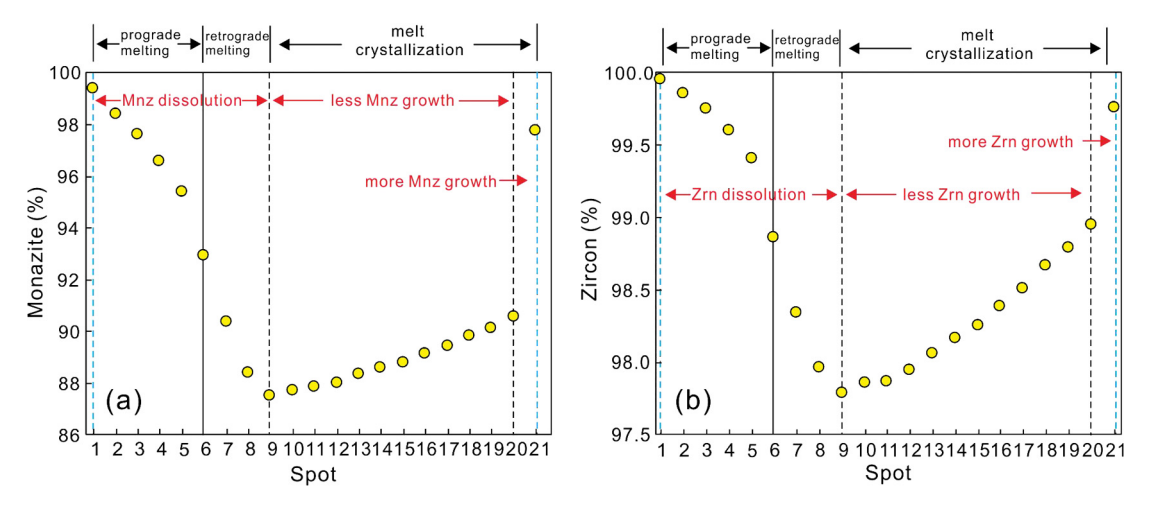


Fig. 9. Calculated amounts of monazite (a) and zircon (b) relative to amounts at the solidus versus the melt content for a metapelite with composition corresponding to sample 111-1 along the calculated P-T path (Fig. 4). These models indicate that the dissolution of monazite and zircon during partial melting (melt increase) and growth upon cooling (melt decrease) are concentrated near the solidus. Calculations are based on Kelsey et al. (2008) with the LREE and Zr contents of 318.6 ppm and 85.0 ppm, respectively (corresponding to sample 111-1). Fig. 4d shows the locations of the calculated points (shown as numbers) where the melt content and mineral modes were calculated.

(Jamieson et al., 2004), while observed P-T paths show heating and loading (Fig. 8). Second, for peak temperatures similar to the Cona rocks, an age of partial melting is predicted to occur at least 30 Myr after the initiation of collision, or ≤30 Ma (Jamieson et al., 2004). In contrast, our work shows much earlier initial melting at 42-40 Ma, similar to data from central Nepal that show temperatures above ca. 700°C by 40 Ma (Kohn and Corrie, 2011; Carosi et al., 2015; Walters and Kohn, 2017). Reconciling T-t paths with south-directed flow between 40 and 20 Ma would require that GHS rocks were much hotter when they accreted, permitting flow as much as 10 Myr earlier (by ca. 40 Ma) and lasting 10 Myr longer than typically assumed. This hypothesis would imply initial south-directed thrusting within the GHS (Carosi et al., 2018 and references therein) and (in most models) north-directed extension along structures such as the STDS as early as 40 Ma. Insofar as we know, no petrochronologically-supported ages as yet indicate such early movement. In addition, if extension along the STDS contributed to the rapid exhumation recorded by the Cona rocks, most extension would have occurred after 24 Ma, consistent with a majority of estimates of the timing of STDS initiation (see Kapp and DeCelles, 2019 and references therein).

6.3. How shear heating and anatexis may regulate thermal structure

Maximum P–T conditions for the upper GHS are well within the partial melting field defined by muscovite dehydration-melting (Fig. 4a). However, because overthrusting cools hanging walls, and because prior subduction should have preconditioned the overriding crust to relatively low temperatures (Kapp and DeCelles, 2019), it is not completely clear how GHS rocks reached these temperatures so early. Consequently, one or more factors must have promoted high temperatures and partial melting.

Many studies have investigated the causes of partial melting, including analytical solutions to the heat flow equation (e.g., England et al., 1992), and numerical models of mid- to lower crustal thrust-sense shear zones (Nabelek et al., 2010). Based on Himalayan boundary conditions, shear heating is viewed as an important source of heat for the GHS and could have raised temperatures in the region of the shear zone by $>200^{\circ}$ C (England et al., 1992; Nabelek et al., 2010). Prior to collision, models predict relatively low temperatures at the base of the crust ($<600^{\circ}$ C; England et al., 1992; Beaumont et al., 2001, 2006; Jamieson et al., 2004; Nabelek et al., 2010) even assuming high radioactive heat production (5μ W/m3) in some models (Faccenda et al., 2008). Cenozoic

ages for Himalayan metamorphism are all less than the timing of collision, so rocks were not close to melting before thickening (also indicated by our calculated P-T path; Fig. 4). To produce melts so soon after initial burial, another source of heat – likely shear heating – must have contributed to the GHS thermal evolution and generation of migmatites.

While England et al. (1992) and Nabelek et al. (2010) show that shear heating can cause partial melting on short time scales, they do not explain how partial melts are maintained on long time scales. Nabelek et al. (2010) hypothesize that rocks could cycle between partial melting, extraction of melts, increased temperature, and partial melting. But, besides the fact that there is no evidence for this process in our rocks (or, for the period 60–25 Ma, for any other section of the GHS that we know of), shear stresses drop dramatically with melt fraction (Rosenberg and Handy, 2005). Consequently, it is unclear how rocks would sustain sufficient shear stress to reach the high temperatures needed to produce extractable melt and sustain the cycle. Instead, we propose that shear heating might drive a feedback among rock strength, melt fraction, and temperature that self-regulates temperature close to the solidus of a rock.

Low temperatures (no melt) correspond with greater rock strength such that shearing can potentially produce heat up to ca. 20 μW/m³ (equivalent to 60 mW/m² for a 3 km-thick shear zone at 700°C with a displacement rate of upper and lower bounds of 3 cm/yr; Nabelek et al., 2010). The consequent increase in temperature would then promote melting that would weaken rocks, produce less heat, and retard any further temperature increase. The lower limit of heat production is difficult to quantify, but for the weakest flow laws could be essentially 0 (Nabelek et al., 2010). That is, shear heating provides a dynamic range of ca. 20 uW/m^3 of heat production (ca. 60 mW/m^2 of heat flux) that could regulate temperature, melt fraction, and rock strength. A negative feedback, in which strong rocks heat and become weaker, whereas weak rocks cool and become stronger, should converge on a condition such that melt fraction was high enough to promote some melt-weakening, but not so high as to eliminate shear heating, e.g., perhaps $5-10~\mu\text{W/m}^3$ of heat production distributed over a 3 km-thick shear zone (15-30 mW/m²) with a few percent partial melt. We note that the viscosity of high-Si melts could inhibit large-scale melt segregation and migration such that melts might not drain from host rocks, although penetrative deformation could form small, foliation-parallel leucosomes as we see in the studied rocks (Appendix Fig. 1). Shearing could occur either ho-

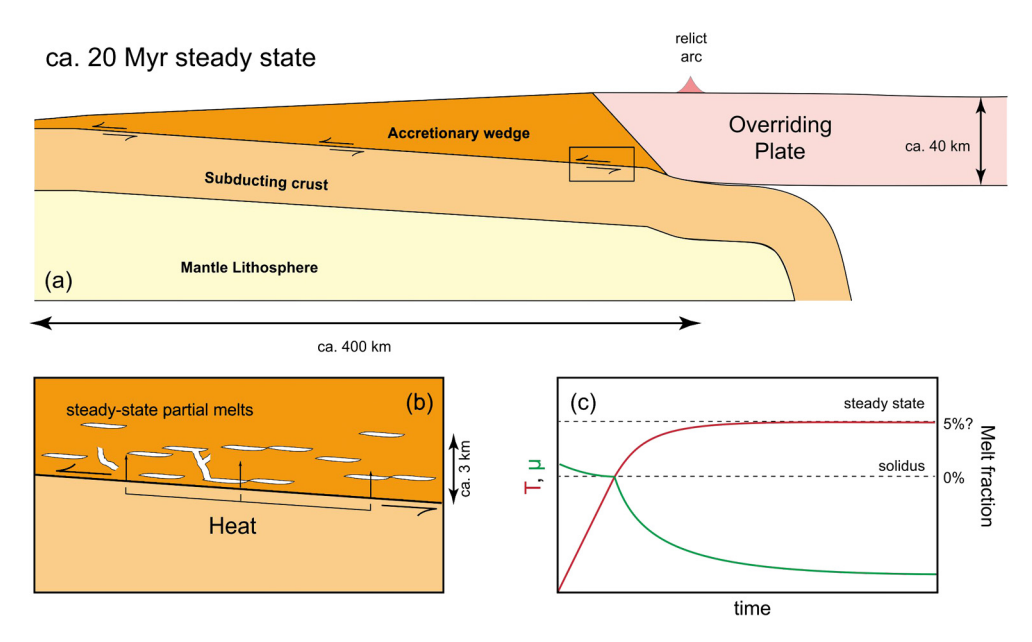


Fig. 10. Mechanism to maintain a small melt fraction over tectonic timescales in a Himalayan-type orogen over time scales up to 20 Myr. (a) Shallow-angle subduction occurs below the accretionary wedge, which, in the Himalaya, would include GHS rocks. (b) Immediately above the interface, shear heating increases temperatures to form a small melt fraction. (c) As temperature (T; red curve) rises, shear stress (μ ; green curve) decreases gradually at temperatures below the solidus, and rapidly decreases at temperatures above the solidus. A small fraction of melt (here hypothesized to be ca. 5%) provides enough shear strength to maintain temperatures at steady state. See text for further discussion.

mogeneously through a several km-thick section or along discrete shears and still produce comparable heat (Nabelek et al., 2010). Because the process is self-regulating, small amounts of melt might persist for millions to tens of millions of years. The amount of melt that permits self-regulation is unknown. At extreme strain rates $(10^{-5}/s)$ at 800° C, rock strength decreases from >800 MPa at 0% melt fraction to ca. 100 MPa at ca. 5% melt fraction and 10 MPa at 20% melt fraction (Rosenberg and Handy, 2005). These experimental results would imply that a melt fraction up to a few tens of percent might be sustainable. However, extrapolation of experiments to geologically plausible strain rates is not yet possible.

Long lasting flat subduction of thinned Indian lithosphere as proposed by Kapp and DeCelles (2019) (Fig. 10a) would drive thrust sense shearing beneath the overriding accretionary wedge of GHS and THS rocks. Shearing at the base of the GHS would have begun at ca. 50-60 Ma during initial collision between THS-GHS rocks and Asia. While temperatures would have been too low to initiate melting at this time, burial and heating of GHS rocks combined with shear heating would drive prograde metamorphism and garnet growth. With continued shearing and radioactive decay, temperatures would eventually exceed the solidus, and melt fraction would steadily increase (Fig. 10b). An increase in melt fraction would decrease rock shear strength, the magnitude of shear heating, and the rate of temperature rise. Eventually the system would reach a steady state in which the amount of shear heating plus radioactive decay would balance heat loss via conduction to maintain a constant temperature (Fig. 10b) and melt fraction (Fig. 10c). Any perturbations to the system would be self-correcting. For example, any melt loss would increase rock strength and shear heating until a similar melt fraction was restored.

6.4. Rapid exhumation and cooling: the arrival of mainland India?

The period 20–25 Ma records a dramatic change in Himalayan deformation and metamorphism, with the development of intra-GHS thrust-sense shear zones such as the HHD, intrusion of numerous Himalayan leucogranites, and initiation of the STDS (Yin and Harrison, 2000; Weinberg, 2016; Carosi et al., 2018; Kapp and

DeCelles, 2019). Subsequent deformation and metamorphism were pervasive throughout the Himalayan orogenic wedge, including the formation of numerous major thrust systems such as the MCT, Ramgarh/Munisari thrust, and Lesser Himalayan duplex, metamorphism of the Lesser Himalayan Sequence, and continued intrusion of leucogranites (e.g., Yin and Harrison, 2000; Kohn, 2014). It is during the 18-24 Ma window that upper GHS rocks from Cona show a rapid decrease in pressure, followed by cooling. Possibly, starting ~24 Ma, a sheet of migmatitic middle crust started to stack along the HHD and perhaps other intra-GHS shear zones (e.g., Carosi et al., 2018) to begin creating the thick GHS sequence that is observed today. While no intra-GHS ductile shear zone has been mapped in the Cona region, such features can be cryptic, and less structural analysis has been conducted immediately to the south. Erosion plus thinning along the STDS could have led to the early rapid exhumation and cooling of the Cona rocks.

van Hinsbergen et al. (2012) argue that the period from 20-25 Ma represents a transition from so-called "soft" collision of either oceanic or thinned continental lithosphere (subduction of either Greater India or the Greater Indian basins) to "hard" collision of thick continental (mainland) Indian lithosphere. Although our data may be viewed as consistent with the Greater India (basins) hypothesis, they do not uniquely distinguish it from other hypotheses. Alternative tectonic hypotheses for the P-T-t history of the studied rocks are difficult to reconcile with shortening estimates. If mainland India was not converging with (accreted) GHS between 40 and 25 Ma, approximately 2000 km of convergence must have been accommodated elsewhere in the orogen. Structural assessments do not identify sufficient shortening along older structures to explain this transport discrepancy, but perhaps older shear zones were active within the GHS since 40 Ma (see Carosi et al., 2018). If so, future research investigating the internal architecture of the GHS might reduce the inferred size of Greater India.

7. Conclusions

Metapelite and felsic gneiss exposed in the Cona area, eastern Himalaya, experienced peak metamorphism with conditions of ca. $720-745^{\circ}\text{C}$ and ca. 9.6-10 kbar, within the field of partial melting.

A reversal in monazite chemistry at 42–40 Ma is interpreted to represent the timing of initial melting, while systematic trends in monazite and zircon chemistry indicate that partial melts persisted until ca. 18 Ma in the upper GHS. Exhumation to ca. 5.5 kbar with slight cooling preceded final melt crystallization.

The mechanism(s) by which melts could form so early and persist for ca. 22–24 Myr are enigmatic. Possibly, feedbacks among shear stress, temperature, melt fraction, and rock strength might self-regulate to sustain a constant melt fraction up to a few tens of Myr. A change from thermal and mechanical stasis to rapid exhumation and cooling at ca. 24 Ma corresponds with an orogen-wide transition to thrusting, leucogranite intrusion, and formation of the STDS and the HHD, and may reflect arrival of mainland India.

CRediT authorship contribution statement

Huixia Ding did all the analysis, prepared context figures and finished the original manuscript. Matthew Kohn proposed the tectonic model, focused on writing and finalised the paper. Zeming Zhang supported all the analysis and revised the original manuscript.

Declaration of competing interest

We declare that we have no financial and personal relationships with other people or organizations that can inappropriately influence our work, there is no professional or other personal interest of any nature or kind in any product, service and/or company that could be construed as influencing the position presented in, or the review of, the manuscript entitled.

Acknowledgements

We thank R. Jamieson and an anonymous reviewer for meticulous and insightful reviews, and A. Yin for editorial handling. This research was co-supported by the National Natural Science Foundation of China (91855210, 41872064 and 41602062), the National Key Research and Development Project of China (2016YFC0600310), the United States National Science Foundation (OIA 1545903, EAR 1450507, and EAR 1918488), and the Fundamental Research Funds for the Central Universities of China (649911026).

Appendix A. Supplementary material

Supplementary material related to this article can be found online at https://doi.org/10.1016/j.epsl.2021.116764.

References

- Aikman, A.B., Harrison, T.M., Ding, L., 2008. Evidence for Early (>44 Ma) Himalayan crustal thickening, Tethyan Himalaya, southeastern Tibet. Earth Planet. Sci. Lett. 274, 14–23.
- Beaumont, C., Jamieson, R.A., Nguyen, M.H., Lee, B., 2001. Himalayan tectonics explained by extrusion of a low-viscosity crustal channel coupled to focused surface denudation. Nature 414. 738–742.
- Beaumont, C., Nguyen, M.H., Jamieson, R.A., Ellis, S., 2006. Crustal flow modes in large hot orogens. Geol. Soc. (Lond.) Spec. Publ. 268, 91–145.
- Carosi, R., Montomoli, C., Iaccarino, S., 2018. 20 years of geological mapping of the metamorphic core across Central and Eastern Himalayas. Earth-Sci. Rev. 177, 124–138.
- Carosi, R., Montomoli, C., Langone, A., Turina, A., Cesare, B., Iaccarino, S., Fascioli, L., Visonà, D., Ronchi, A., Rai, S.M., 2015. Eocene partial melting recorded in peritectic garnets from kyanite-gneiss, Greater Himalayan Sequence, central Nepal. Geol. Soc. (Lond.) Spec. Publ. 412, 111–129.
- Cook, K.L., Royden, L.H., 2008. The role of crustal strength variations in shaping orogenic plateaus, with application to Tibet. J. Geophys. Res., Solid Earth 113, B08407.

- Cottle, J.M., Larson, K.P., Kellett, D.A., 2015. How does the mid-crust accommodate deformation in large, hot collisional orogens? A review of recent research in the Himalayan orogen. J. Struct. Geol. 78, 119–133.
- Ding, H.X., Zhang, Z.M., 2016. Neoproterozoic granitoids in the eastern Himalayan orogen and their tectonic implications. Precambrian Res. 285, 1–9.
- Ding, H.X., Zhang, Z.M., Dong, X., Tian, Z.L., Xiang, H., Mu, H.C., Gou, Z.B., Shui, X.F., Li, W.C., Mao, L.J., 2016. Early Eocene (c. 50 Ma) collision of the Indian and Asian continents: constraints from the North Himalayan metamorphic rocks, southeastern Tibet. Earth Planet. Sci. Lett. 435. 64–73.
- Ding, H.X., Zhang, Z.M., Li, M.M., Niu, Z.X., Zhang, N., 2017. Metamorphism and tectonic significance of the Greater Himalayan Crystalline Sequence in Cona region, eastern Himalaya. Acta Petrol. Sin. 33, 2357–2376.
- England, P., Le Fort, P., Molnar, P., Pêcher, A., 1992. Heat sources for Tertiary metamorphism and anatexis in the Annapurna-Manaslu region (central Nepal). J. Geophys. Res. 97, 2107–2128.
- Faccenda, M., Gerya, T.V., Chakraborty, S., 2008. Styles of post-subduction collisional orogeny: influence of convergence velocity, crustal rheology and radiogenic heat production. Lithos 103, 257–287.
- Goscombe, B., Gray, D., Hand, M., 2006. Crustal architecture of the Himalayan metamorphic front in eastern Nepal. Gondwana Res. 10, 232–255.
- Guillot, S., Maheo, G., de Sigoyer, J., Hattori, K.H., Pecher, A., 2008. Tethyan and Indian subduction viewed from the Himalayan high-to ultrahigh-pressure metamorphic rocks. Tectonophysics 451, 225–241.
- Harlov, D.E., Wirth, R., Hetherington, C.J., 2011. Fluid-mediated partial alteration in monazite: the role of coupled dissolution-reprecipitation in element redistribution and mass transfer. Contrib. Mineral. Petrol. 162, 329–348.
- Harrison, T.M., Grove, M., Lovera, O.M., Catlos, E.J., 1998. A model for the origin of Himalayan anatexis and inverted metamorphism. J. Geophys. Res. 103, 27017–27032.
- Henry, D.J., Guidotti, C.V., Thomson, J.A., 2005. The Ti-saturation surface for low-to-medium pressure metapelitic biotites: implications for geothermometry and Ti-substitution mechanisms for geothermometry and Ti-substitution mechanisms. Am. Mineral. 90, 316–328.
- Hu, X.M., Garzanti, E., Moore, T., Raffi, I., 2015. Direct stratigraphic dating of India–Asia collision onset at the Selandian (middle Paleocene, 59 ± 1 Ma). Geology 43, 859-862.
- Iaccarino, S., Montomoli, C., Carosi, R., Massonne, H.J., Langone, A., Visona, D., 2015. Pressure-temperature-time-deformation path of kyanite-bearing migmatitic paragneiss in the Kali Gandaki valley (central Nepal): investigation of Late Eocene-Early Oligocene melting processes. Lithos 231, 103–121.
- Jamieson, R.A., Beaumont, C., Medvedev, S., Nguyen, M.H., 2004. Crustal channel flows; 2, numerical models with implications for metamorphism in the Himalayan–Tibetan Orogen. J. Geophys. Res. 109, B06407.
- Jamieson, R.A., Unsworth, M.J., Harris, N.B.W., Rosenberg, C.L., Schulmann, K., 2011. Crustal melting and the flow of mountains. Elements 7, 251–258.
- Jurewicz, S.R., Watson, E.B., 1985. Distribution of partial melt in a felsic system: the importance of surface energy. Contrib. Mineral. Petrol. 85, 25–29.
- Kapp, P., DeCelles, P.G., 2019. Mesozoic-Cenozoic geological evolution of the Himalayan-Tibetan orogen and working tectonic hypotheses. Am. J. Sci. 319, 159–254.
- Kelsey, D.E., Clark, C., Hand, M., 2008. Thermobarometric modelling of zircon and monazite growth in melt-bearing systems: examples using modal metapelitic and metapsammitic granulites. J. Metamorph. Geol. 26, 199–212.
- Kirkland, C.L., Whitehouse, M.J., Slagstad, T., 2009. Fluid-assisted zircon and monazite growth within a shear zone: a case study from Finnmark, Arctic Norway. Contrib. Mineral. Petrol. 158, 637–657.
- Kohn, M.J., 2014. Himalayan metamorphism and its tectonic implications. Annu. Rev. Earth Planet. Sci. 42, 381–419.
- Kohn, M.J., Corrie, S., 2011. Preserved Zr-temperatures and U-Pb ages in high-grade metamorphic titanite: evidence for a static hot channel in the Himalayan orogen. Earth Planet. Sci. Lett. 311, 136–143.
- Kohn, M.J., Wieland, M., Parkinson, C.D., Upreti, B.N., 2004. Miocene faulting at plate tectonic velocity in the Main Central thrust region, central Nepal. Earth Planet. Sci. Lett. 228, 299–310.
- Kohn, M.J., Wieland, M.S., Parkinson, C.D., Upreti, B.N., 2005. Five generations of monazite in Langtang gneisses: implications for chronology of the Himalayan metamorphic core. J. Metamorph. Geol. 23, 399–406.
- Koziol, A.M., 1989. Recalibration of the garnet-plagioclase-Al₂SiO₅-quartz (GASP) geobarometer and application to natural parageneses. Eos Trans. AGU 70, 493.
- Larson, K.P., Ambrose, T.K., Webb, A.A.G., Cottle, J.M., Shrestha, S., 2015. Reconciling Himalayan midcrustal discontinuities: the Main Central thrust system. Earth Planet. Sci. Lett. 429, 139–146.
- Le Fort, P., 1975. Himalayas: the collided range. Present knowledge of the continental arc. Am. J. Sci. 275A, 1–44.
- Martin, A.J., Gehrels, G.E., DeCelles, P.G., 2007. The tectonic significance of (U, Th)/Pb ages of monazite inclusions in garnet from the Himalaya of central Nepal. Chem. Geol. 244, 1–24.
- Montomoli, C., Carosi, R., Iaccarino, S., 2015. Tectonometamorphic discontinuities in the Greater Himalayan Sequence: a local or a regional feature? Geol. Soc. (Lond.) Spec. Publ. 412. 25–41.

- Nabelek, P.I., Whittington, A.G., Hofmeister, A.M., 2010. Strain heating as a mechanism for partial melting and ultrahigh temperature metamorphism in convergent orogens: implications of temperature-dependent thermal diffusivity and rheology. J. Geophys. Res. 115, B12417.
- Najman, Y., Appel, E., Boudagher-Fadel, M., Bown, P., Carter, A., Garzanti, E., Godin, L., Han, J., Liebke, U., Oliver, G., 2010. Timing of India-Asia collision: geological, biostratigraphic, and palaeomagnetic constraints. J. Geophys. Res. 115, B12416.
- Nelson, K.D., Zhao, W.J., Brown, L.D., Kuo, J., Che, J.K., Liu, X.W., Klemperer, S.L., Makovsky, Y., Meissner, R., Mechie, J., Kind, R., Wenzel, F., Ni, J., Nabelek, J., Chen, L.S., Tan, H.D., Wei, W.B., Jones, A.G., Booker, J., Unsworth, M., Kidd, W.S.F., Hauck, M., Alsdorf, D., Ross, A., Cogan, M., Wu, C.D., Sandvol, E., Edwards, M., 1996. Partially molten middle crust beneath southern Tibet: Synthesis of Project INDEPTH results. Science 274, 1684–1688.
- Pyle, J.M., Spear, F.S., 2003. Four generations of accessory-phase growth in low-pressure migmatites from SW New Hampshire. Am. Mineral. 88, 338–351.
- Rosenberg, C.L., Handy, M.R., 2005. Experimental deformation of partially melted granite revisited: implications for the continental crust. J. Metamorph. Geol. 23, 19–28.
- Rubatto, D., 2002. Zircon trace element geochemistry: distribution coefficients and the link between U-Pb ages and metamorphism. Chem. Geol. 184, 123–138.
- Rubatto, D., Chakraborty, S., Dasgupta, S., 2013. Timescale of crustal melting in the higher Himalayan crystallines (Sikkim, eastern Himalaya) inferred from trace element-constrained monazite and zircon chronology. Contrib. Mineral. Petrol. 165, 349–372.
- Spear, F.S., Kohn, M.J., Florence, F., Menard, T., 1991. A model for garnet and plagioclase growth in pelitic schists: implications for thermobarometry and P-T path determinations. J. Metamorph. Geol. 8, 683–696.

- Teyssier, P.F., Whitney, D.L., 2002. Extension rates, crustal melting, and core complex dynamics. Geology 37, 391–394.
- van Hinsbergen, D.J.J., Lippert, P.C., Dupont-Nivet, G., McQuarrie, N., Doubrovine, P.V., Spakman, W., Torsvik, T.H., 2012. Greater India basin hypothesis and a twostage Cenozoic collision between, India and Asia. Proc. Natl. Acad. Sci. USA 109, 7659–7664
- Walters, J.B., Kohn, M.J., 2017. Protracted thrusting followed by late rapid cooling of the Greater Himalayan Sequence, Annapurna Himalaya, central Nepal: insights from titanite petrochronology. J. Metamorph. Geol. 35, 897–917.
- Wang, J.M., Rubatto, D., Zhang, J.J., 2015. Timing of partial melting and cooling across the Greater Himalayan Crystalline Complex (Nyalam, Central Himalaya): in-sequence thrusting and its implications. J. Petrol. 56, 1677–1702.
- Weinberg, R.F., 2016. Himalayan leucogranites and migmatites: nature, timing and duration of anataxis. J. Metamorph. Geol. 34, 821–843.
- Yin, A., Dubey, C.S., Kelty, T.K., Webb, A.A.G., Harrison, T.M., Chou, C.Y., Célérier, J., 2010. Geologic correlation of the Himalayan orogen and Indian craton: part 2. Structural geology, geochronology, and tectonic evolution of the Eastern Himalaya. Geol. Soc. Am. Bull. 122, 360–395.
- Yin, A., Harrison, T.M., 2000. Geologic evolution of the Himalaya-Tibetan orogeny. Annu. Rev. Earth Planet. Sci. 28, 211–280.
- Zhang, Z.M., Xiang, H., Dong, X., Ding, H.X., He, Z.Y., 2015. Long-lived high-temperature granulite-facies metamorphism in the Eastern Himalayan orogen, south Tibet. Lithos 212–215, 1–15.